# Geophysical Research Letters®

**Key Points:**

- Extreme positive Indian Ocean Dipole (EXpIOD) cooling can be classified into an equatorial type, as seen in 2023/1997, and a coastal type
- Strong El Niño extends EXpIOD cooling equatorially by enhancing central Indian Ocean easterlies and ensuing nonlinear vertical advection
- The shaping effect of strong El Niño on co-occurring EXpIOD is confirmed in century-long observations and coupled model simulations

**Correspondence to:**

L. Zhang and J.-Z. Wang,
zhanglei@scsio.ac.cn;
jia-zhen_wang@foxmail.com

# Exceptional Equatorial Extension of Extreme Indian Ocean Dipole Cooling: Shaping Effect From Strong El Niño

**Mingmei Xie[1], Jia-Zhen Wang[1], Lei Zhang[2] [iD], and Zhaohui Chen[1] [iD]**

[1]Frontier Science Center for Deep Ocean Multispheres and Earth System, and Physical Oceanography Laboratory, Ocean University of China, Qingdao, China, [2]State Key Laboratory of Tropical Oceanography, South China Sea Institute of Oceanology, Chinese Academy of Sciences, Guangzhou, China

**Abstract** The extreme positive Indian Ocean Dipole (EXpIOD) peaking in 2023 boreal fall exhibited the strongest variations in sea level and subsurface temperature in the eastern Indian Ocean (IO), and the most equatorially westward extension of cooling observed during the satellite era to date. Its pattern resembled the 1997 EXpIOD, contrasting with other coastally-concentrated EXpIODs. Here we show that the distinctive air-sea responses of equatorial EXpIODs stem from the energetic central IO zonal winds fueled by concurrent strong El Niños, which were absent in other cases. The exceptionally strong easterly anomaly generates prominent nonlinear vertical advection cooling the central IO, with nonlinear zonal advection and the Ekman feedback playing supportive roles. Current coupled models can capture this Pacific shaping effect, despite with divergent strengths. Under strong El Niño's inter-basin forcing, the westward extension of cooling has profound implications for regional hydrology and coral ecology, and warrants closer attention in future predictions.

**Plain Language Summary** The Indian Ocean Dipole (IOD) is the dominant interannual variability of the tropical Indian Ocean (TIO) during boreal fall. In its positive phase, cold sea surface temperature anomalies (SSTAs) develop off the coasts of Sumatra and Java, while warm SSTAs occur in the western basin. Extreme positive IOD events (EXpIODs), characterized by intense eastern cooling, garner scientific community attention due to their substantial impacts on the hydrological and ecological systems of TIO-rim countries. In this study, we identify that the eastern cold tongue of EXpIODs, as the core of IOD evolution, generally exhibits two shapes—equatorially-extended and coastally-concentrated. The equatorially-extended EXpIOD features far westward reach of the eastern cooling, along with intensified anomalous easterlies. Strong El Niño events, concurrent with these equatorially-extended EXpIODs but absent in those coastally-concentrated ones, amplify the central Indian Ocean easterlies through the atmospheric bridge, resulting in pronounced cold nonlinear vertical advection to reinforce the former type. This inter-basin regulation between climate modes is also detected in century-long observations and coupled model simulations. Our results suggest that although the co-occurrence of strong El Niño and EXpIOD is coincidental, once they co-occur, strong El Niño could effectively shape the structure of EXpIOD and magnify its climate impacts.

## 1. Introduction

The positive phase of the Indian Ocean Dipole (pIOD) features an anomalous zonal sea surface temperature (SST) gradient across the equatorial Indian Ocean (Saji et al., 1999; Webster et al., 1999), as depicted by high positive values of the dipole mode index (DMI; IODW (50°E−70°E, 10°S–10°N) minus IODE (90°E−110°E, 10°S–0°)) (Saji et al., 1999). The IOD typically emerges during the boreal summer and reaches peak intensity in fall (September-October-November; SON). Synthesizing from previous studies, extreme pIOD (EXpIOD) events occurred in the years 1994, 1997, 2006, 2019 and 2023 since the 1980s as global satellite observations became available (Cai et al., 2021; J.-Z. Wang et al., 2024; Figure S1 in Supporting Information S1), and in 1961 and 1877 prior to this modern observational era (Abram et al., 2008; Gooding, 2022; Singh et al., 2018). Unlike moderate pIOD (MpIOD) events, which generally exhibit comparable and modest amplitudes at each pole or a dominant warming in the west (Cai et al., 2021; Jiang et al., 2022), EXpIOD events are marked by strong cooling over the eastern Indian Ocean (EIO) extending from the Sumatra coast (Cai et al., 2021; J.-Z. Wang et al., 2024). This pronounced eastern cooling manifests the EIO as a pacemaker for driving the IOD's evolution and climate impacts (Lee et al., 2022; Zhao & Nigam, 2014). It has been projected that EXpIOD events will become more frequent under anthropogenic warming (Cai et al., 2014, 2021; J.-Z. Wang et al., 2024), appealing for a deeper understanding on these extremes.

Although it was forecasted in advance as a positive event (Bureau of Meteorology, 2023), the 2023 IOD reaching such extreme levels, just 4 years after the 2019 event, was unexpected. Hydrological impacts during the 2023 EXpIOD introduced several distinctive characteristics compared to its predecessors. This event caused the return of intense drought and smoky wildfires in Indonesia after several comparatively calm fire seasons (Hansen, 2023; Jong, 2024), resulting in the lowest domestic rice production in the past decade (USDA, 2023). Droughts and heatwaves also swept over Australia, with burnt areas and carbon emissions estimated to be the highest since 2012 (CAMS, 2024; Fisher, 2024). On the other side of the basin, East Africa experienced an unprecedented series of heavy rains in late 2023, which abruptly shifted the region's longest-recorded drought (2020 to early 2023) into devastating floods (Cassidy, 2023). In both Kenya and Somalia, the floods were reported as the most severe in decades (Sheikh, 2023; Wright, 2023), comparable to 1997 and much worse than other EXpIOD years (Wain-wright et al., 2021). Severe flooding has killed over 1,900 people and forced more than 10 million people to flee their homes (ICRC, 2024; IFRC, 2024; UNOCHA, 2023). Given these catastrophic consequences, it is worthy of investigating the potential causes that made the 2023 event's climate impacts stand out from others.

The El Niño-Southern Oscillation (ENSO)–IOD connection has been a long-standing debate in IOD studies (Annamalai et al., 2003; Ashok et al., 2003; Fischer et al., 2005; Li et al., 2003; Stuecker et al., 2017; J.-Z. Wang & Wang, 2021; Zhao & Nigam, 2014; L. Zhang, Han, et al., 2021, Zhang, Wang, et al., 2021). The near-neutral ENSO state observed in 1961 and 2019 clearly declared that EXpIOD events can be triggered by Indian Ocean internal processes (for example, equatorial waves and the Madden-Julian Oscillation (MJO); Du et al., 2020; Han et al., 2006; Z. Huang et al., 2022; L. Zhang, Han, & Hu, 2021), as well as other ambient climate variabilities (for example, monsoons and interhemispheric sea level pressure gradient; Annamalai et al., 2003; Sun et al., 2015; Lu & Ren, 2020), so that they could develop independently of ENSO.

On the other hand, ENSO and IOD are physically connected through the Walker Circulation, thereby significant correlations existing between them. Extensive experiments done by a hierarchy of models have successfully produced dipole-like responses over the Indian Ocean to ENSO forcing (e.g., Annamalai et al., 2003; Li et al., 2003; L. Zhang, Han, & Hu, 2021). With ENSO diversity considered, the inter-basin relationship is particularly robust for the stronger eastern Pacific (EP) El Niño (W. Zhang et al., 2015), whereas the central Pacific (CP) El Niño–IOD relation is more sensitive to the shapes (X. Wang & Wang, 2014) and zonal center positions of the CP anomalies (L. Zhang, Han, & Hu, 2021; W. Zhang et al., 2015), which, however, may be disrupted when some special CP cases are included (Z. Huang et al., 2022). Thus, the ENSO–IOD inter-basin connection has yet to be fully understood. Inspired by the distinct EXpIOD spatial patterns in 2023 and 1997, and their concurring ENSO events (see Sections 3.1 and 3.3), here we demonstrate a regulating effect of strong EP El Niño events on the westward intrusion of EXpIOD cooling along the equator from observational and modeling evidences. Our finding highlights the need of incorporating reasonable inter-basin interaction pathway to accurately predict the EXpIOD patterns and the severity of associated disasters.

## 2. Data and Methods

In this study, we used the monthly Optimally Interpolated Reynolds SST version 2.1 (OISSTv2.1, B. Huang et al., 2021) and HadSST4.0.1 (Kennedy et al., 2019) to examine SST variations during EXpIOD events. The observed rainfall data were sourced from the CPC Merged Analysis of Precipitation (CMAP; P. Xie & Arkin, 1997). Contemporaneous atmospheric conditions were provided by the ECMWF Reanalysis v5 (ERA5; Hersbach et al., 2020). Oceanic variables were analyzed with the usage of the Estimating the Circulation and Climate of the Ocean v2 (ECCO2; Menemenlis et al., 2008) and NCEP Global Ocean Data Assimilation System (GODAS; Behringer & Xue, 2004). Anomalies were calculated relative to the climatology of the entire data set period and then linearly detrended, except for the HadSST4.0.1, which was quadratically detrended due to its span starting from 1850.

We conducted a *K*-means cluster analysis (MacQueen, 1967) to provide a statistical basis for the grouping of IOD events. The *K*-means clustering is designed to partition a given multi-dimensional data into *K* clusters under the constraint of minimizing the sum of intra-cluster distance. Here the Manhattan distance was used. We included three essential variables—SSTA extent, zonal current, and subsurface temperature—that are integrally involved in the Bjerknes feedback into the clustering, which yields two distinct EXpIOD groups (see Section 3.1). We further diagnosed the mixed-layer heat budget to reveal the associated mechanisms as follows:

$$\langle T'_t \rangle = -\left( \langle \overline{w} T'_z \rangle + \langle w' \overline{T}_z \rangle + \langle w' T'_z \rangle \right) - \left( \langle \overline{\mathbf{u}}_h \cdot \nabla_h T' \rangle + \langle \mathbf{u}'_h \cdot \nabla_h \overline{T} \rangle + \langle \mathbf{u}'_h \cdot \nabla_h T' \rangle \right) + Q'_{net} + \text{Res.}, \tag{1}$$

where $\langle T \rangle$ represents the mixed-layer temperature (MLT), a proxy for SST; $\mathbf{u}_h$ and $w$ denote horizontal and vertical velocities, respectively; $\nabla_h$ and $*_z$ are the horizontal and vertical gradient operators, respectively; the overbar ($\overline{*}$) and prime ($*'$) indicate climatological-mean and anomalous fields, respectively; $\langle * \rangle$ denotes the vertical average operator ($\frac{1}{H}\int_{-H}^{0} * \, dz$). The mixed layer depth is defined as the depth at which potential density changes by 0.125 kg m$^{-3}$ relative to the sea surface. $Q_{net}$ stands for the net surface heat flux (positive downward), which is the sum of shortwave, longwave, latent heat, and sensible heat fluxes, divided by $\rho_w C_p \overline{H}$ ($\rho_w = 1{,}025$ kg m$^{-3}$ and $C_p = 3{,}986$ J kg$^{-1}$°C$^{-1}$), so that it has the same unit (°C month$^{-1}$) as all the other heat budget terms. Note that the shortwave radiation escaped from the base of the mixed layer has been subtracted based on a penetration parameterization scheme (Paulson & Simpson, 1977). For advection terms within each bracket, the first two terms are linear advections involving mean currents or mean temperature gradients, while the last term represents nonlinear advection that transports temperature anomalies via anomalous currents. The residual term (Res.) includes vertical and lateral mixing, entrainment, and nonlinear effects resulting from sub-monthly and sub-grid processes.

To increase the sample size of EXpIOD events and demonstrate the role of concurrent ENSO, we analyzed two sets of Coupled Model Intercomparison Project Phase 6 (CMIP6)-class coupled global circulation model (CGCM) experiments. The first set included tropical Pacific pacemaker experiments from CESM2 (1880–2019; 10 members; CESM CVCWG, 2022) and FGOALS-f3-L (1870–2014; 10 members; Hu et al., 2022), in which SSTAs were restored to the observed monthly anomalies over the EP and allowed to evolve freely elsewhere. In such experiment, strong EP El Niño events (SON Niño3 (150°W–90°W, 5°S–5°N) > 2 s.d.; 7 years in CESM2 and 7 years in FGOALS-f3-L were identified) were consistent in timing, pattern, and intensity with the historical records, while EXpIOD episodes were generated sporadically and spontaneously through the model's internal air-sea interactions. Whether EXpIOD events coinciding with prescribed strong El Niño signal or not forms two contrasting scenarios, providing an ideal bisection for testing the Pacific modulation effect. The second set of CGCM experiments comprised the pre-industrial control (piControl) simulations from 32 CMIP6 models (Eyring et al., 2016; Table S1 in Supporting Information S1). The multi-century simulation periods therein ensure that the identified significant EXpIOD–strong EP El Niño connection does not stem from sampling randomness.

## 3. Results

### 3.1. Characteristics-Based Grouping of EXpIOD Events

A pIOD event is identified when the observed DMI exceeds 0.5 standard deviations (s.d.). For an extreme event, the threshold is raised to 1.5 s.d. During the period of 1982–2023, five EXpIOD and seven MpIOD events were selected accordingly (Figure S1 in Supporting Information S1). Given the substantial variations of the western warming center across pIOD events (Endo & Tozuka, 2016; Lee et al., 2022; Zhao & Nigam, 2014), our focus is primarily on the characteristics in the central to eastern basin. After the stratified DMI selection, we further performed a $K$-means cluster analysis using three additional metrics: the longitudinal position where the SSTA crosses zero along the equator, the zonal ocean current anomaly in the central Indian Ocean ($u'$; CIO; 70°E–90°E, 5°S–5°N), and the subsurface temperature anomaly in the EIO ($T'_{sub}$; 85°E–110°E, 5°S–0°). This analysis resulted in two distinct groups within the EXpIOD regime, apart from the MpIOD which exhibits much weaker air-sea interactions (Figure S2 in Supporting Information S1).

The first group of EXpIOD events, comprising the 2023 and 1997 events, is characterized by a pronounced westward extension of the tongue-like EIO cooling along the equator (Figures 1a and 1d), accompanied by energetic westward winds and flows (Figures 1a and 1e). Hence, it is termed the "equatorial EXpIOD." This group is underpinned by an extensive and intense subsurface cooling, forming a deeply penetrated anomalous system (Figures 1a and 1f), with the 2023 event ranking as the most severe to date. In contrast, the second group, which includes the 1994, 2006, and 2019 events, features the EIO cooling generally concentrated in the vicinity of the Sumatra–Java coast, expanding offshore toward the southwest (Figure 1b). Consequently, its subsurface counterpart is also weaker (Figures 1d–1f). Here we refer to this group as the "coastal EXpIOD." Clustering based solely on SSTAs in the central-eastern Indian Ocean yields consistent classification results in observational data (Figure S3 in Supporting Information S1) and, when applied to CMIP6 piControl experiments, similarly identifies
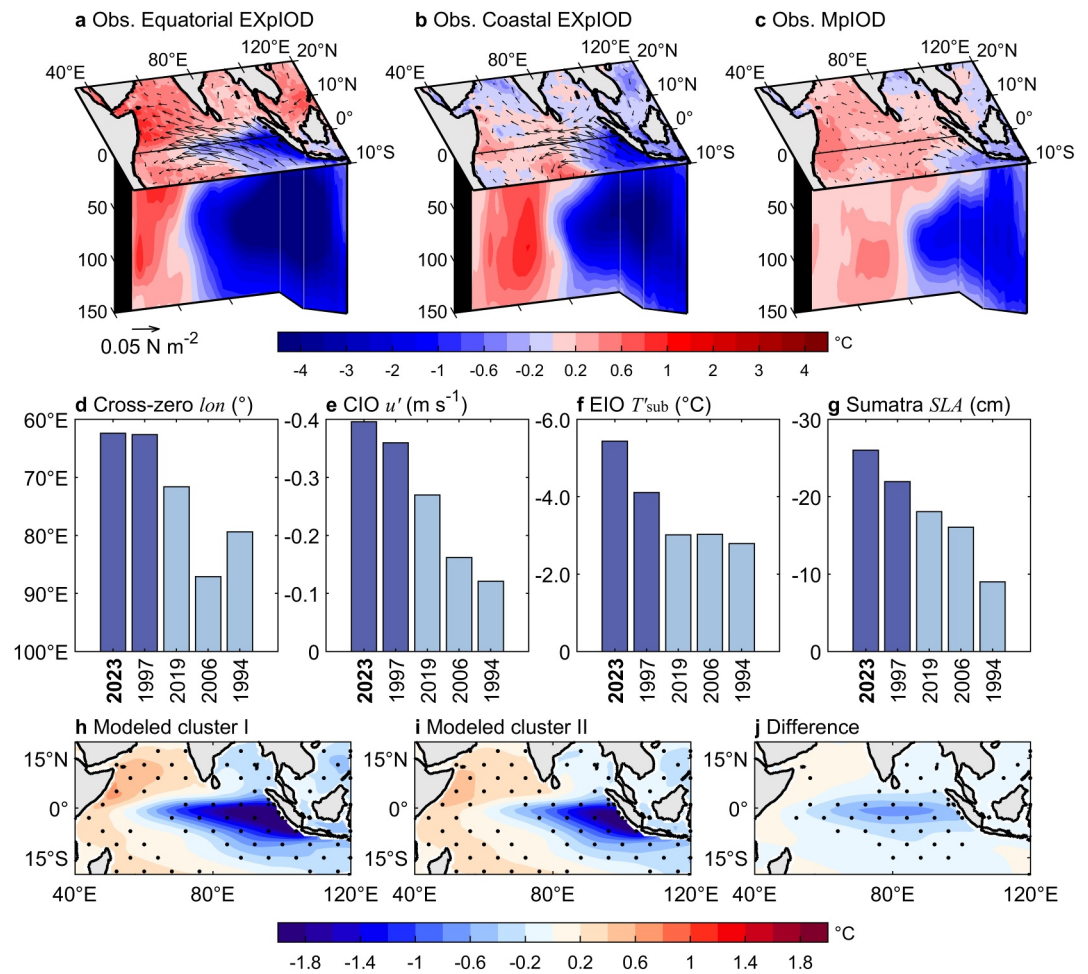
**Figure 1.** Characteristics of the three pIOD categories after clustering. (a) SON SSTAs (shading; °C), subsurface temperature anomalies along the equator (averaged within 2°S–2°N) and the Sumatra–Java coastline (averaged over a 2° offshore region), and surface wind stress anomalies (vectors; N m$^{-2}$) during the observed equatorial EXpIOD. (b) As in panel (a), but for the coastal EXpIOD. (c) As in panel (a), but for the MpIOD. (d–g) Key indicators for the air-sea responses during EXpIOD events: (d) the longitudinal position where SSTAs cross zero along the equator; (e) the zonal ocean current anomaly in the CIO ($u'$; 70°E−90°E, 5°S–5°N); (f) the subsurface temperature anomaly in the EIO ($T'_{sub}$; 85°E−110°E, 5°S–0°); and (g) the sea level anomaly off the Sumatra coast ($SLA$; 90°E−100°E, 8°S–0°). $K$-means clustering for SSTAs (50°−110°E; 10°S–10°N) over the central-eastern Indian Ocean during EXpIOD events in the CMIP6 piControl experiments: (h) Cluster I, (i) Cluster II, and (j) their difference. EXpIOD events (IODE cooling >1.5 s.d.) selected from models are pre-classified, a priori, into two categories based on the number of the observed division. The dotted area indicates regions where 80% of the models exhibit the same sign. The spatial differences are more prominent in the CIO rather than along the coast of Sumatra.

distinct EXpIOD types (Figures 1h–1j). This refined classification could provide a clearer understanding on their differentiated characteristics and underlying mechanisms.

Distinctions also exist in many other aspects of the air-sea coupled system. During equatorial EXpIOD events, the westward intrusion of SSTAs and zonal wind anomalies (Figure 1a) drives an anomalous dry tongue wedging into the western basin, displacing convection further west toward East Africa (Figures S4a and S4c in Supporting Information S1). In contrast, coastal EXpIOD events show a shift in zonal winds from easterly to westerly anomalies near 60°E (Figure 1b), anchoring the convergence zone mainly over the ocean rather than the African continent (Figure S4b in Supporting Information S1). This difference helps to explain why more severe floods are triggered by equatorial EXpIOD events (Figure S4d in Supporting Information S1). Furthermore, the westward extended dry tongue and enhanced East African rainfall in equatorial EXpIOD composite remain evident even after removing the direct, linear effects of Niño3 and IODW through partial regression (Figure S5 in Supporting Information S1).

The energetic westward flows in the CIO during equatorial EXpIODs result from the anomalously stronger easterly winds aloft, which also trigger a sequence of equatorial upwelling Kelvin waves that raise the thermocline in the EIO and lower sea levels off Sumatra (Figure 1g). Additionally, these anomalous easterly winds and their curl induce downwelling off-equatorial Rossby waves that propagate westward, leading to intense subsurface warming (50–100 m) occupying the Seychelles–Chagos thermocline ridge region (SCTR; 50°E−80°E, 5°S–12°S; Figure S6a in Supporting Information S1). Extreme variations like those observed during the 2023 and 1997 equatorial EXpIOD events have inflicted significant damage on coral reef ecosystems across the basin. Drastic sea level drops in the EIO extend the exposure time of shallow-water coral reefs to direct sunlight, exacerbating their vulnerability (Dunne et al., 2021; van Woesik, 2004). Meanwhile, subsurface warming in the SCTR imposes intense thermal stress on mesophotic corals—valuable but fragile ecosystems inhabiting low-light environments at depths of 30–150 m (Rocha et al., 2018)—triggering severe bleaching events (Diaz et al., 2023). Taken together, the equatorial EXpIOD effectively activates the Indian Ocean air-sea coupled system compared to coastal EXpIOD events, thereby leaving imprints on multiple variables and posing more profound threats on the health and resilience of human communities and ecosystems in the rim regions.

### 3.2. Dominant Processes for Equatorial Extension and Strong El Niño's Shaping Effect

The MLT tendency ($T_t'$) of equatorial EXpIOD events in August closely resembles that of coastal events, indicating that the key processes differentiating equatorial EXpIOD events from others have not yet occurred (Figures S7a and S7b in Supporting Information S1). However, distinctions between the two become evident in September. The cooling tendency of coastal events significantly weakens, while equatorial events experience an intensification of cooling near Sumatra, which also extends westward, forming a narrow band along the equator and thrusting into the west of 70°E (Figures S7c and S7d in Supporting Information S1). By October, the cooling tendency of equatorial EXpIODs remains strong, suggesting continued growth. In contrast, the MLT tendency of coastal EXpIODs returns to a neutral state, signifying their maturity (Figures S7e and S7f in Supporting Information S1). As it turns to November, for both equatorial and coastal events, the EIO is occupied by warming tendency, indicating a transition to the EXpIOD decay phase (Figures S7g and S7h in Supporting Information S1). Thus, it is the pronounced cooling anomalies during the September–October (SO) season, both alongshore enhanced and equatorially extended, that distinguish the equatorial EXpIOD from other EXpIOD events (Figure 2a).

Further diagnosis reveals that nonlinear vertical advection ($-w'T_z'$) is the primary driver for the equatorial EXpIOD cooling (Figure 2a), as evidenced by their great spatial overlap (comparing Figure 2b with Figure S7c in Supporting Information S1). This nonlinear vertical advection is shaped by anomalous upwelling ($w'$), which is equatorially and coastally trapped, so that it emerges as an elongated cooling stripe and acts to upwell intense subsurface cold anomalies into the mixed layer (Figure 2b). The second contributor is nonlinear zonal advection ($-u'T_x'$; Figure 2a), the zonal component of $-\mathbf{u}_h' \cdot \nabla_h T'$. Due to the relatively uniform distribution of zonal anomalous currents along the equator, nonlinear zonal advection is stronger where the temperature gradient is sharp (e.g., near the cross-zero longitude; Figure 2c). This process favors the westward intrusion of the EIO cold tongue by transporting cooling anomalies toward the African continent. The growth of $-w'T_z'$ and $-u'T_x'$ from September to October aligns with their inherent nonlinear dependence on the anomaly fields, thus amplifying as the event develops (Figures S8a and S8b in Supporting Information S1).

The Ekman feedback ($-w'\overline{T}_z$), whose strength grows modestly from September to October (Figures S8a and S8b in Supporting Information S1), shares a similar spatial distribution with the total cooling tendency but is weaker in amplitude, thereby playing a less important role (Figures 2a and 2d). The effect of the thermocline feedback ($-\overline{w}T_z'$) hinges on the direction of climatological vertical motions. Due to the monsoon transition and the consequent onset of the fall Yoshida-Wyrtki jet (Han et al., 1999; Wyrtki, 1973; Yoshida, 1959), the equatorial mean upwelling shifts to downwelling (Figure S9 in Supporting Information S1) and thus the thermocline feedback diminishes from September to October, creating a meridional warming-cooling dipole structure with a near-zero net contribution to the westward extension (Figures 2a and 2e). The residuals for both types of EXpIOD events show similar signs and amplitudes, suggesting they behave similarly across event types and contribute minimally to the differences in cooling patterns. In contrast, the terms $-w'T_z'$, $-u'T_x'$, and $-w'\overline{T}_z$ differ significantly between the two types, with amplitudes much larger than those of the residual terms, underpinning their important shaping effects (Figure 2a).
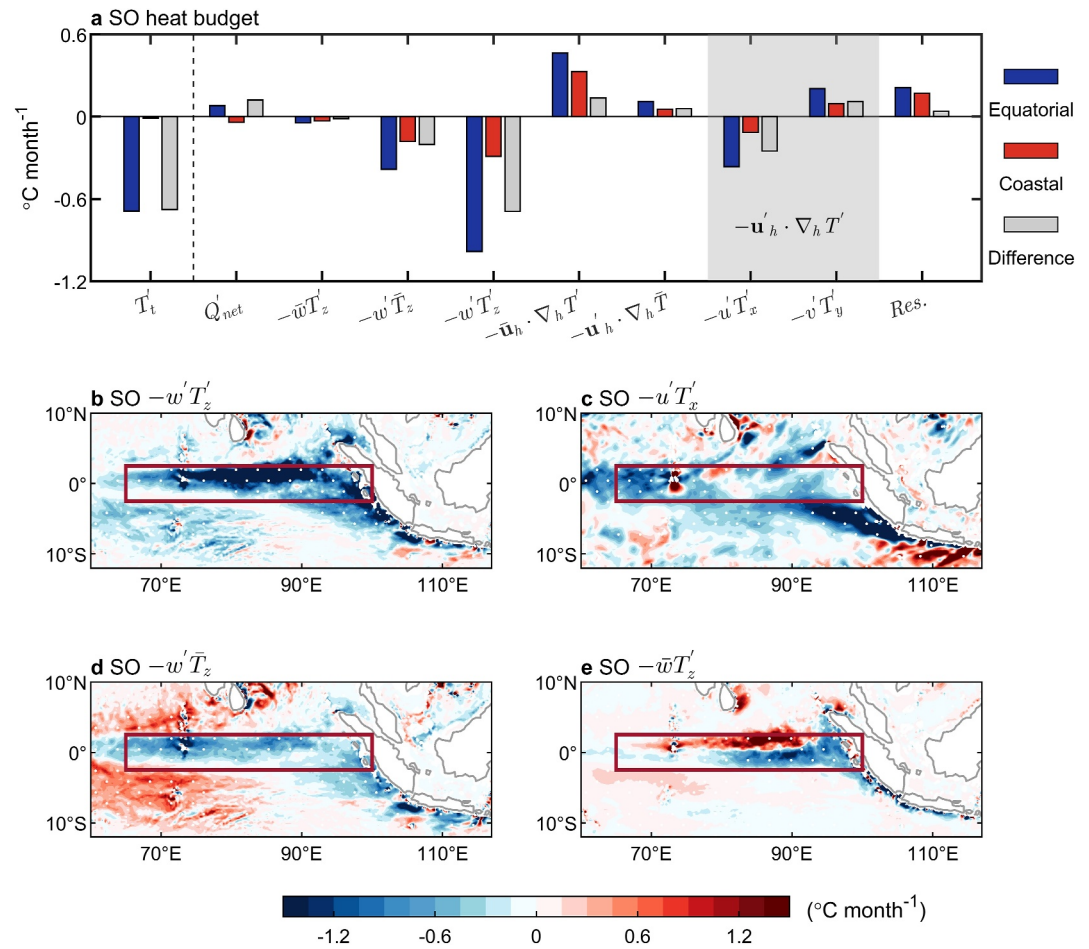
**Figure 2.** Heat budget in the SO season. (a) Mixed layer heat budget terms (°C month$^{-1}$) during equatorial and coastal EXpIOD events and their differences, averaged over the equatorial central–eastern Indian Ocean (65°E–100°E, 2.5°S–2.5°N; red boxes in panels (b–e)). The gray shading marks the zonal and meridional components of $-\mathbf{u}'_h \cdot \nabla_h T'$. (b–e) Spatial distributions of (b) nonlinear vertical advection ($-w'T'_z$), (c) nonlinear zonal advection ($-u'T'_x$), (d) the Ekman feedback ($-w'\overline{T}_z$) and (e) the thermocline feedback ($-\overline{w}T'_z$). The white dots indicate locations where all cases have the same sign.

Physically, the intensities of $w'$, $u'$ and $T'_z$ are all linked to the variation of CIO zonal winds. Dynamical responses to an enhanced easterly anomaly typically include westward acceleration of surface currents, surface meridional Ekman divergence and upwelling on the equator, and a spectrum of equatorial waves (Cane, 1980; Moore & Philander, 1977; Nyadjro & McPhaden, 2014), with the cold, eastward-propagating Kelvin wave being particularly influential in accumulating subsurface cooling and transmitting the upwelling signal toward the Sumatra–Java island chain.

A close inspection on the relation between EIO cooling and CIO zonal wind shows that the coastal events along with other non-EXpIOD years constitute a linear regression line, whereas the two equatorial events (2023 and 1997) clearly deviate from it (Figure 3a). This deviation remains evident even when the regression is changed from linear to quadratic (Figure S10a in Supporting Information S1), suggesting that additional processes are at play in amplifying the CIO winds, beyond the internal coupling within the Indian Ocean. Additionally, the deviation is apparent in boreal fall but not in summer (Figure S10b in Supporting Information S1), further supporting that crucial for reshaping the EXpIOD cooling extent is the late development stage. The most notable difference in the concurrent global SSTAs lies in the presence of intense Pacific El Niño warming during equatorial EXpIOD events, which is absent in coastal events (Figures 3b and 3c). The directly forced effect of
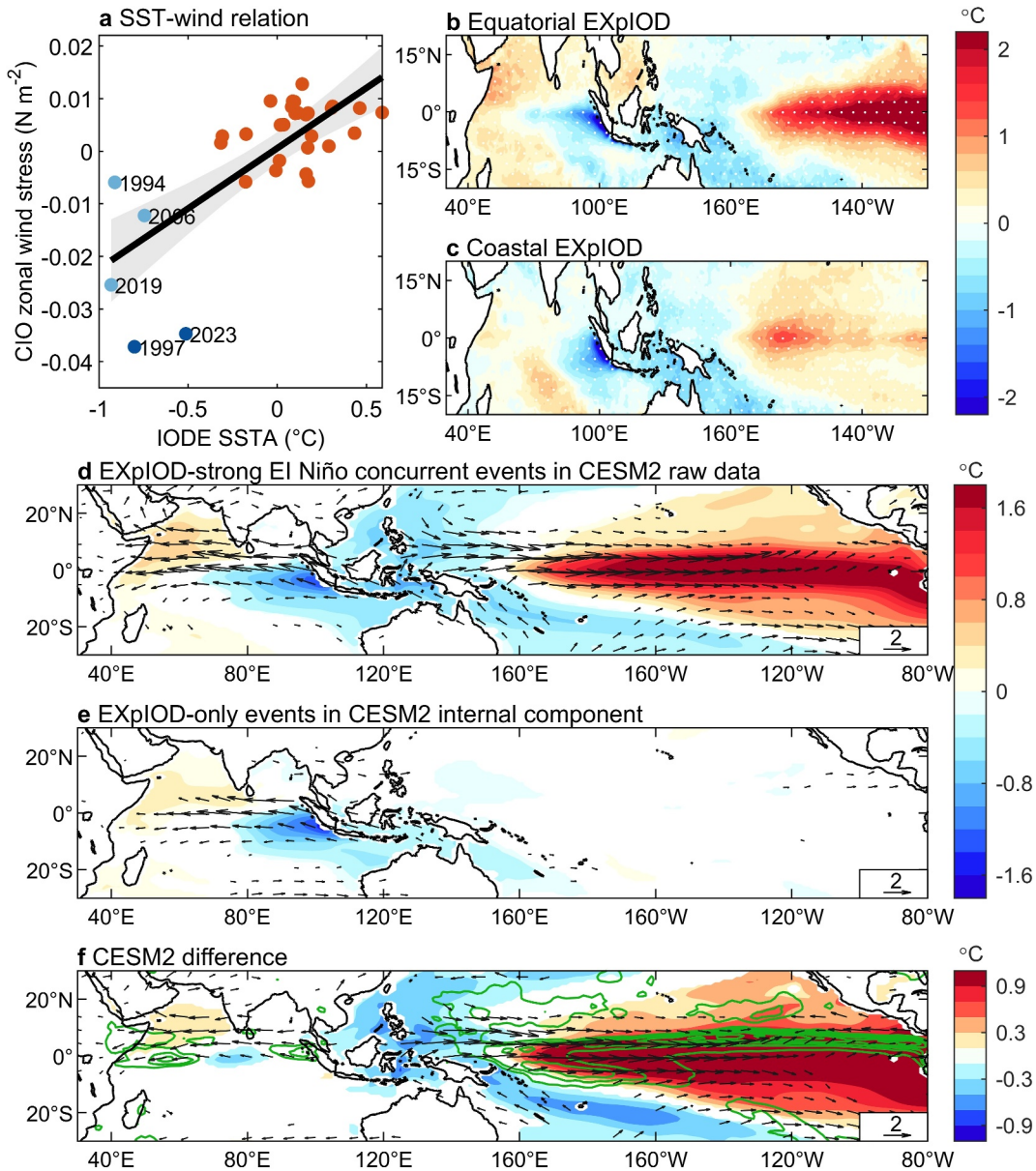
**Figure 3.** Shaping effect on EXpIOD events from the concurrent strong El Niño. (a) Relationship between the IODE SSTA and the CIO zonal wind stress from 1982 to 2023 in observations. The linear regression (black line) and its 95% confidence intervals (gray shading) are shown. (b) Composite SSTAs (°C) over the Indo–Pacific region during observed equatorial EXpIOD events. (c) As in panel (b), but for coastal EXpIOD events. The white dots indicate locations where all cases have the same sign. (d) Composite SSTAs of concurrent EXpIOD–strong El Niño events in the raw data of the CESM2 pacemaker experiment. These events are defined by the intersection of EXpIODs (IODE cooling >1.5 s.d.) and strong El Niños (Niño3 index >2 s.d.). In the raw data, both internal-coupling-generated and Pacific-forced signals are present. Thus, the former can be modulated by the latter. (e) As in panel (d), but for EXpIOD events in the internal component of the CESM2 pacemaker experiment, where the Pacific-forced signal is largely removed, as indicated by the absence of significant values over the tropical Pacific. Thus, EXpIOD events therein could be regarded in an unforced state. (f) The difference between (d and e). Green contours represent significant positive differences in rainfall anomalies, with intervals of 1 mm day$^{-1}$. In panel (d–f), only SSTAs (shading; °C) and 850-hPa winds (vectors; m s$^{-1}$) significant at the 90% confidence level (based on a two-tailed $t$-test) are shown.

strong El Niño years is examined using the ensemble-mean of the CESM2 Pacific pacemaker experiment. It shows that enhanced convection over the Pacific could result in divergence over the Maritime Continent and easterly anomalies across the equatorial Indian Ocean, clearly indicating the connectivity between the two basins via the atmospheric bridge (Figure S11 in Supporting Information S1).

### 3.3. Strong El Niño–Equatorial EXpIOD Connection in Longer Observations and CGCMs

The post-1980 period manifests an increased frequency of EXpIOD events compared to the previous century (J.-Z. Wang et al., 2024). By extending the analysis back to 1850 with the HadSST4.0.1 data set, only two additional EXpIOD events are identified—those in 1877 and 1961. Notably, the 1877 EXpIOD coincided with an exceptionally strong El Niño in the Pacific (Figure S12a in Supporting Information S1; see also B. Huang et al., 2020), while the 1961 EXpIOD occurred during a near-neutral to cold ENSO phase (Figure S12b in Supporting Information S1). An evident difference in the cooling extent between these two events is observed, with the 1877 EXpIOD extending farther west than the 1961 event (comparing black dots in Figures S12a and S12b in Supporting Information S1), again validating the shaping effect of strong El Niño on the EXpIOD structure.

However, despite this shaping effect, a strong El Niño alone cannot determine whether EXpIOD will happen, as revealed by the lack of a one-to-one correspondence between them in observational records. So is the case in the CESM2 pacemaker experiment. We decomposed the Pacific-forced component from total variabilities (raw data) as the mean across all members, and treated the deviations from the ensemble mean as the internal component not associated with ENSO. The strong El Niño-forced IODE cooling (i.e., the mean of all strong El Niño cases) is only 0.74 s.d., far below the EXpIOD threshold of 1.5 s.d. As such, modeled EXpIOD events may occur with the prescribed strong El Niño by chance or develop independently via internal coupling.

Therefore, we further selected those events co-occurring with strong El Niño in raw data (16 cases in total) as the first group, where the internally-generated signal is regulated by strong El Niño (Figure 3d), and selected EXpIOD events in the internal component (14 cases in total) as the second group, in which the Pacific effect is largely removed (Figure 3e). The Indian Ocean cold SSTA of the first group stretches from the Sumatra–Java coast to the far west, with strong easterlies prevailing over the basin, consistent with the configuration of equatorial EXpIOD (Figure 3d). In contrast, the cold SSTA in the second group is less westward-extended (Figure 3e). Their difference shows intense warming over the Pacific and cold residuals over the CIO, accompanied by excessive rainfall over East Africa (Figure 3f). A similar contrast holds for the FGOALS-f3-L pacemaker experiment (Figure S13 in Supporting Information S1). A minor drawback is that the statistically significant CIO cooling contrast appears less prominent than observed, likely due to the common model bias of excessive extension of the simulated IOD's eastern pole, leading to an overextension in these internally generated events as well.

To confirm that this shaping effect is not peculiar to a small subset of CGCMs, we used the CMIP6 multi-model piControl experiments. Since each model has only one realization, decomposition into forced and internal components, as done in pacemaker experiments, is not possible. However, the multi-century to millennium-long simulations provide a large number of EXpIOD events (i.e., IODE cooling >1.5 s.d.) to assess the influence of ENSO. We identified the intrusion longitude of cooling along the equator for each case and then selected the upper 25% and the lower 25% in each model to differentiate between equatorially-extended and coastally-concentrated cases (Figures 4a and 4b). The differences in SSTAs over the CIO and the Pacific between the two groups follow a linear relationship (Figure 4d), indicating that models' ability to distinguish between the equatorially-extended and the coastally-concentrated EXpIOD events largely depends on how well they simulate the amplitude contrast in the accompanying Pacific El Niño events (Figure 4c).

## 4. Summary and Discussion

The extraordinary equatorially westward extension of cooling during the 2023 and 1997 boreal falls, along with energetic zonal currents and intense subsurface temperature anomalies, elevated these two EXpIOD events to a status that transcends all other coastally-concentrated EXpIOD and MpIOD events observed to date. Accordingly, East Africa experienced extreme rainfall and coral ecosystems faced severe thermal stress in these years. Analysis reveals that the distinction in evolution between equatorial and coastal EXpIODs becomes pronounced in the SO season, the late stage of development. Cold nonlinear vertical advection, driven by strong easterly anomalies, predominantly creates an equatorial cooling band with the help of nonlinear zonal advection and the Ekman feedback, leading to the excessive westward intrusion of equatorial EXpIODs. Beyond the Indian Ocean internal processes, the concurrent strong El Niño state is essential to generate the exceptionally strong easterly anomalies via the anomalous Walker circulation, which induces low-level divergence over the Maritime Continent and establishes a pressure gradient across the tropical Indian Ocean basin. Extending the
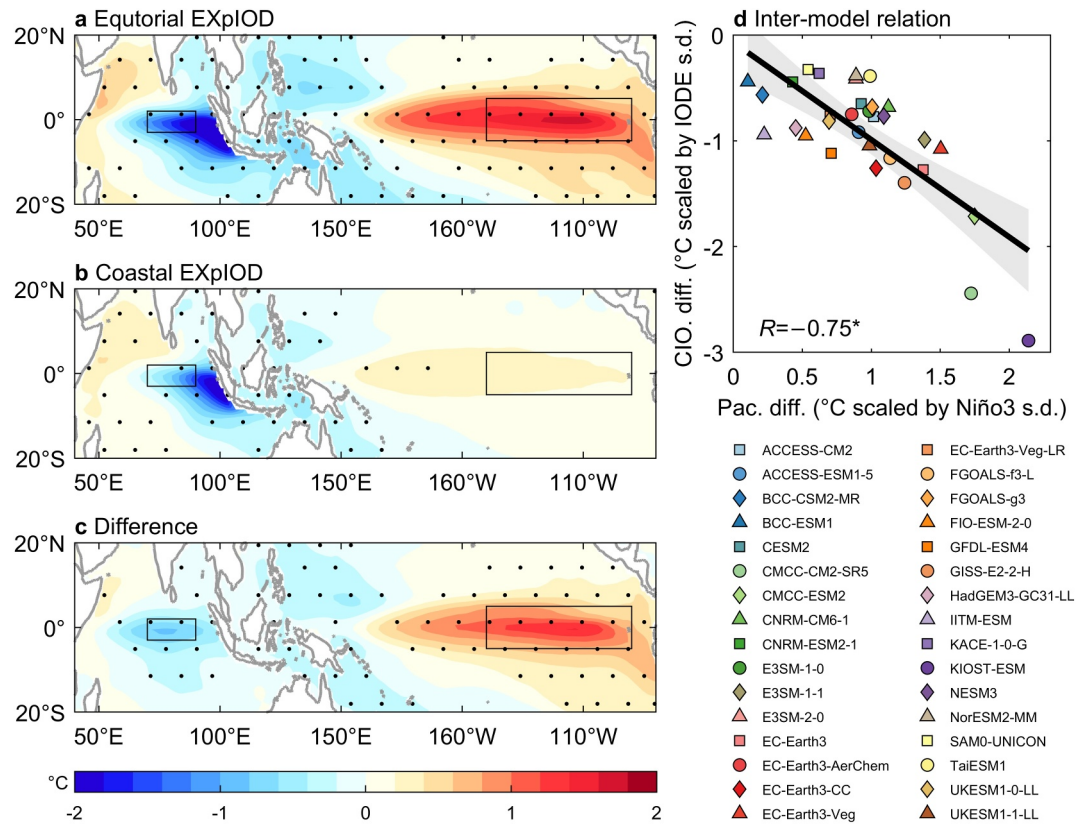
**Figure 4.** Contrasting equatorial and coastal EXpIOD events in the CMIP6 piControl experiment. Composite SSTAs for (a) equatorial EXpIOD events, (b) coastal EXpIOD events and (c) their difference. The position of EXpIOD westward intrusion is indicated by the longitude where cold SSTAs along the equator decay to the e-folding of 1 s.d. of IODE SSTA. Equatorial EXpIOD events are defined as those in the upper 25%, while coastal EXpIOD events fall into the lower 25%. The dotted area indicates regions where 80% of the models exhibit the same sign. (d) Inter-model relationship between the strength difference in concurrent El Niño signals (Niño3 region) and the strength difference in cooling intrusion over the CIO (70°E−90°E, 4°S–2°N). Varying the threshold of identifying intrusion longitude from 0.1 to 0.4 s.d. and the percentile defining EXpIOD groups from 20% to 33% does not qualitatively alter the conclusion.

analysis to century-long observations and simulations, we find that EXpIODs form two distinct groups based on their concurrence with strong El Niño, with the paired events exhibiting a more notable westward cooling compared to EXpIOD-only events. As the severity of climate impacts on surrounding natural and socio-economic systems is highly dependent on the EXpIOD pattern, model predictions would benefit from faithfully reproducing strong El Niño's inter-basin forcing and its shaping effect.

Based on current evidence, it is worth noting that: (a) While strong El Niño can influence the extent of EXpIOD cooling, it does not necessarily make the IODE cooling of equatorial events stronger than that of coastal events. Observations show that their mean intensities are comparable (−0.70°C vs. −0.85°C; x-axis in Figure 3a), and in both pacemaker and piControl experiments, the difference representing the Pacific effect is more pronounced over the CIO rather than off the Sumatra–Java coast (Figures 3f and 4c, and Figure S13c in Supporting Information S1). (b) A strong El Niño by itself cannot turn a pIOD event into an extreme one from scratch; rather, it serves as a regulator and booster. The occurrence of EXpIOD is an outcome of interactions across multiple timescales and factors, with ENSO being one of them. For example, the 2023 event was staged by exceptionally strong MJO activities in phases 8 and 1 during the March–April season, which built up significant subsurface signals conducive to the onset of pIOD (Figure S14 in Supporting Information S1). However, this was not sufficient to distinguish the 2023 event by the end of summer (see x-axis in Figure S10b in Supporting Information S1), when the co-occurring strong El Niño began to work in relay, amplifying the EXpIOD intensity and extending its cooling extent during the late development stage.

## Data Availability Statement

All data used in this study are publicly available. OISSTv2.1 (B. Huang et al., 2021), CMAP (P. Xie & Arkin, 1997) and GODAS (Behringer & Xue, 2004) data are from the NOAA (https://psl.noaa.gov/data/gridded/data.noaa.oisst.v2.highres.html, https://psl.noaa.gov/data/gridded/data.cmap.html, https://psl.noaa.gov/data/gridded/data.godas.html). HadSST4.0.1 data (Kennedy et al., 2019) are from the UK Met Office Hadley Centre (https://www.metoffice.gov.uk/hadobs/hadsst4/). ECCO2 (Menemenlis et al., 2008) data are produced by the NASA JPL and are downloaded from the APDRC (https://apdrc.soest.hawaii.edu/datadoc/ecco2_cube92.php). ERA5 data (Hersbach et al., 2020) are from the Copernicus Climate Data Store (https://cds.climate.copernicus.eu/datasets/reanalysis-era5-single-levels-monthly-means?tab=download). The CMIP6 model outputs (Eyring et al., 2016) are from the ESGF (https://aims2.llnl.gov/search). The daily real-time multivariate MJO (RMM) indices (Wheeler & Hendon, 2004) are from the Australian Bureau of Meteorology (http://www.bom.gov.au/climate/mjo/#tabs=Monitoring).

## References

Abram, N. J., Gagan, M. K., Cole, J. E., Hantoro, W. S., & Mudelsee, M. (2008). Recent intensification of tropical climate variability in the Indian Ocean. *Nature Geoscience*, *1*(12), 849–853. https://doi.org/10.1038/ngeo357

Annamalai, H., Murtugudde, R., Potemra, J., Xie, S. P., Liu, P., & Wang, B. (2003). Coupled dynamics over the Indian Ocean: Spring initiation OF the zonal mode. *Deep Sea Research Part II: Topical Studies in Oceanography*, *50*(12), 2305–2330. https://doi.org/10.1016/S0967-0645(03)00058-4

Ashok, K., Guan, Z., & Yamagata, T. (2003). A look at the relationship between the ENSO and the Indian Ocean dipole. *Journal of the Meteorological Society of Japan. Ser. II*, *81*(1), 41–56. https://doi.org/10.2151/jmsj.81.41

Behringer, D. W., & Xue, Y. (2004). Evaluation of the global ocean data assimilation system at NCEP: The Pacific Ocean [Dataset]. *Paper presented at the Eighth Symposium on Integrated Observing and Assimilation Systems for Atmosphere, Oceans, and Land Surface, Seattle, WA.* https://www.researchgate.net/publication/228856991_Evaluation_of_the_global_ocean_data_assimilation_system_at_NCEP_The_Pacific_Ocean

Bureau of Meteorology. (2023). Climate driver update history climate drivers in the Pacific, Indian and Southern Oceans and the Tropics. *Climate Driver Update history*. Retrieved from http://www.bom.gov.au/climate/enso/wrap-up/archive/20230411.archive.shtml

Cai, W., Santoso, A., Wang, G., Weller, E., Wu, L., Ashok, K., et al. (2014). Increased frequency of extreme Indian Ocean Dipole events due to greenhouse warming. *Nature*, *510*(7504), 254–258. https://doi.org/10.1038/nature13327

Cai, W., Yang, K., Wu, L., Huang, G., Santoso, A., Ng, B., et al. (2021). Opposite response of strong and moderate positive Indian Ocean Dipole to global warming. *Nature Climate Change*, *11*(1), 27–32. https://doi.org/10.1038/s41558-020-00943-1

CAMS. (2024). 2023: A year of intense global wildfire activity. *Copernicus Atmosphere Monitoring Service*. Retrieved from https://atmosphere.copernicus.eu/2023-year-intense-global-wildfire-activity

Cane, M. (1980). On the dynamics of equatorial currents, with application to the Indian Ocean. *Deep-Sea Research Part A Oceanographic Research Papers*, *27*(7), 525–544. https://doi.org/10.1016/0198-0149(80)90038-2

Cassidy, E. (2023). Devastating flooding in East Africa, NASA. Retrieved from https://earthobservatory.nasa.gov/images/152108/devastating-flooding-in-east-africa

CESM CVCWG. (2022). CESM2 Pacific pacemaker ensemble instructions. Retrieved from https://www.cesm.ucar.edu/working-groups/climate/simulations/cesm2-pacific-pacemaker/instructions

Diaz, C., Foster, N. L., Attrill, M. J., Bolton, A., Ganderton, P., Howell, K. L., et al. (2023). Mesophotic coral bleaching associated with changes in thermocline depth. *Nature Communications*, *14*(1), 6528. https://doi.org/10.1038/s41467-023-42279-2

Du, Y., Zhang, Y., Zhang, L.-Y., Tozuka, T., Ng, B., & Cai, W. (2020). Thermocline warming induced extreme Indian Ocean Dipole in 2019. *Geophysical Research Letters*, *47*(18), e2020GL090079. https://doi.org/10.1029/2020GL090079

Dunne, R. P., Brown, B. E., Phongsuwan, N., & Putchim, L. (2021). The Indian Ocean dipole and El Niño southern oscillation as major drivers of coral cover on shallow reefs in the Andaman sea. *Global Change Biology*, *27*(14), 3312–3323. https://doi.org/10.1111/gcb.15640

Endo, S., & Tozuka, T. (2016). Two flavors of the Indian Ocean dipole. *Climate Dynamics*, *46*(11), 3371–3385. https://doi.org/10.1007/s00382-015-2773-0

Eyring, V., Bony, S., Meehl, G. A., Senior, C. A., Stevens, B., Stouffer, R. J., & Taylor, K. E. (2016). Overview of the coupled model Inter-comparison project phase 6 (CMIP6) experimental design and organization [Dataset]. *Geoscientific Model Development*, *9*(5), 1937–1958. https://doi.org/10.5194/gmd-9-1937-2016

Fischer, A. S., Terray, P., Guilyardi, E., Gualdi, S., & Delecluse, P. (2005). Two independent triggers for the Indian Ocean dipole/zonal mode in a coupled GCM. *Journal of Climate*, *18*(17), 3428–3449. https://doi.org/10.1175/JCLI3478.1

Fisher, R. (2024). Vastly bigger than the black summer: 84 million hectares of northern Australia burned in 2023. *The Conversation*. Retrieved from https://theconversation.com/vastly-bigger-than-the-black-summer-84-million-hectares-of-northern-australia-burned-in-2023-227996

Gooding, P. (2022). ENSO, IOD, drought, and floods in equatorial eastern Africa, 1876–1878. In P. Gooding (Ed.), *Droughts, floods, and global climatic anomalies in the Indian Ocean World* (pp. 259–287). Springer International Publishing.

Han, W., McCreary, J. P., Anderson, D. L. T., & Mariano, A. J. (1999). Dynamics of the eastern surface jets in the equatorial Indian Ocean. *Journal of Physical Oceanography*, *29*(9), 2191–2209. https://doi.org/10.1175/1520-0485(1999)029<2191:DOTESJ>2.0.CO;2

Han, W., Shinoda, T., Fu, L.-L., & McCreary, J. P. (2006). Impact of atmospheric intraseasonal oscillations on the Indian Ocean Dipole during the 1990s. *Journal of Physical Oceanography*, *36*(4), 670–690. https://doi.org/10.1175/JPO2892.1

Hansen, K. (2023). Indonesian fires return in 2023, NASA. Retrieved from https://earthobservatory.nasa.gov/images/151929/indonesian-fires-return-in-2023

Hersbach, H., Bell, B., Berrisford, P., Hirahara, S., Horányi, A., Muñoz-Sabater, J., et al. (2020). The ERA5 global reanalysis [Dataset]. *Quarterly Journal of the Royal Meteorological Society*, *146*(730), 1999–2049. https://doi.org/10.1002/qj.3803

Hu, S., Wu, B., Zhou, T., & Yu, Y. (2022). Dominant anomalous circulation patterns of Tibetan plateau summer climate generated by ENSO-forced and ENSO-independent teleconnections. *Journal of Climate*, *35*(5), 1679–1694. https://doi.org/10.1175/JCLI-D-21-0207.1

Huang, B., L'Heureux, M., Hu, Z.-Z., Yin, X., & Zhang, H.-M. (2020). How significant was the 1877/78 El Niño? *Journal of Climate*, *33*(11), 4853–4869. https://doi.org/10.1175/JCLI-D-19-0650.1

Huang, B., Liu, C., Banzon, V., Freeman, E., Graham, G., Hankins, B., et al. (2021). Improvements of the daily optimum interpolation sea surface temperature (DOISST) version 2.1 [Dataset]. *Journal of Climate*, *34*(8), 2923–2939. https://doi.org/10.1175/JCLI-D-20-0166.1

Huang, Z., Zhang, W., Liu, C., & Stuecker, M. F. (2022). Extreme Indian Ocean Dipole events associated with El Niño and Madden–Julian oscillation. *Climate Dynamics*, *59*(7–8), 1953–1968. https://doi.org/10.1007/s00382-022-06190-8

ICRC. (2024). The ICRC response to the El Niño flooding in Somalia: October 2023-January 2024, ReliefWeb. Retrieved from https://reliefweb.int/report/somalia/icrc-response-el-nino-flooding-somalia-october-2023-january-2024

IFRC. (2024). Kenya, Africa: Floods 2023 operation update (MDRKE058), ReliefWeb. Retrieved from https://reliefweb.int/report/kenya/kenya-africa-floods-2023-operation-update-mdrke058

Jiang, J., Liu, Y., Mao, J., Li, J., Zhao, S., & Yu, Y. (2022). Three types of positive Indian Ocean dipoles and their relationships with the South Asian summer monsoon. *Journal of Climate*, *35*(1), 405–424. https://doi.org/10.1175/JCLI-D-21-0089.1

Jong, H. N. (2024). As fires ravaged Indonesia in 2023, some positive trends emerged. *Mongabay Environmental News*. Retrieved from https://news.mongabay.com/2024/04/as-fires-ravaged-indonesia-in-2023-some-positive-trends-emerged-data-show/

Kennedy, J. J., Rayner, N. A., Atkinson, C. P., & Killick, R. E. (2019). An ensemble data set of sea surface temperature change from 1850: The Met Office Hadley Centre HadSST.4.0.0.0 data set [Dataset]. *Journal of Geophysical Research: Atmospheres*, *124*(14), 7719–7763. https://doi.org/10.1029/2018JD029867

Lee, S.-K., Lopez, H., Foltz, G. R., Lim, E.-P., Kim, D., Larson, S. M., et al. (2022). Java–Sumatra Niño/Niña and its impact on regional rainfall variability. *Journal of Climate*, *35*(13), 4291–4308. https://doi.org/10.1175/JCLI-D-21-0616.1

Li, T., Wang, B., Chang, C.-P., & Zhang, Y. (2003). A theory for the Indian Ocean dipole–zonal mode. *Journal of the Atmospheric Sciences*, *60*(17), 2119–2135. https://doi.org/10.1175/1520-0469(2003)060<2119:ATFTIO>2.0.CO;2

Lu, B., & Ren, H.-L. (2020). What caused the extreme Indian Ocean Dipole event in 2019? *Geophysical Research Letters*, *47*(11), e2020GL087768. https://doi.org/10.1029/2020GL087768

MacQueen, J. (1967). Some methods for classification and analysis of multivariate observations. Paper presented at the Proceedings of the fifth Berkeley symposium on mathematical statistics and probability.

Menemenlis, D., Campin, J.-M., Heimbach, P., Hill, C., Lee, T., Nguyen, A., et al. (2008). ECCO2: High resolution global ocean and sea ice data synthesis [Dataset]. *Mercator Ocean Quarterly Newsletter*, *31*(October), 13–21. https://www.researchgate.net/publication/253471797_ECCO2_High_Resolution_Global_Ocean_and_Sea_Ice_Data_Synthesis

Moore, D. W., & Philander, S. G. H. (1977). Modelling of the tropical oceanic circulation. In E. D. Goldberg (Ed.), *The Sea* (Vol. 6, pp. 319–361). Wiley-Interscience.

Nyadjro, E. S., & McPhaden, M. J. (2014). Variability of zonal currents in the eastern equatorial Indian Ocean on seasonal to interannual time scales. *Journal of Geophysical Research: Oceans*, *119*(11), 7969–7986. https://doi.org/10.1002/2014JC010380

Paulson, C. A., & Simpson, J. J. (1977). Irradiance measurements in the upper ocean. *Journal of Physical Oceanography*, *7*(6), 952–956. https://doi.org/10.1175/1520-0485(1977)007<0952:IMITUO>2.0.CO;2

Rocha, L. A., Pinheiro, H. T., Shepherd, B., Papastamatiou, Y. P., Luiz, O. J., Pyle, R. L., & Bongaerts, P. (2018). Mesophotic coral ecosystems are threatened and ecologically distinct from shallow water reefs. *Science*, *361*(6399), 281–284. https://doi.org/10.1126/science.aaq1614

Saji, N. H., Goswami, B. N., Vinayachandran, P. N., & Yamagata, T. (1999). A dipole mode in the tropical Indian Ocean. *Nature*, *401*(6751), 360–363. https://doi.org/10.1038/43854

Sheikh, A. (2023). Worst floods in decades kill 29 in Somalia, hit towns across East Africa. *Reuters*. Retrieved from https://www.reuters.com/world/africa/worst-floods-decades-kill-29-somalia-hit-towns-across-east-africa-2023-11-08/

Singh, D., Seager, R., Cook, B. I., Cane, M., Ting, M., Cook, E., & Davis, M. (2018). Climate and the global famine of 1876–78. *Journal of Climate*, *31*(23), 9445–9467. https://doi.org/10.1175/JCLI-D-18-0159.1

Stuecker, M. F., Timmermann, A., Jin, F.-F., Chikamoto, Y., Zhang, W., Wittenberg, A. T., et al. (2017). Revisiting ENSO/Indian Ocean Dipole phase relationships. *Geophysical Research Letters*, *44*(5), 2481–2492. https://doi.org/10.1002/2016GL072308

Sun, S., Lan, J., Fang, Y., & Gao, X. (2015). A triggering mechanism for the Indian Ocean dipoles independent of ENSO. *Journal of Climate*, *28*(13), 5063–5076. https://doi.org/10.1175/JCLI-D-14-00580.1

UNOCHA. (2023). Somalia: 2023 Deyr season floods situation report No. 5. *UNOCHA Report*. Retrieved from https://www.unocha.org/publications/report/somalia/somalia-2023-deyr-season-floods-situation-report-no-5-24-december-2023

USDA. (2023). Indonesia rice area, yield and production. *Crop explorer country summary for major crop regions by the USDA Foreign Agricultural Service*. Retrieved from https://ipad.fas.usda.gov/countrysummary/Default.aspx?id=ID&crop=Rice

van Woesik, R. (2004). Comment on "coral reef death during the 1997 Indian Ocean Dipole linked to Indonesian wildfires". *Science*, *303*(5662), 1297. https://doi.org/10.1126/science.1091983

Wainwright, C. M., Finney, D. L., Kilavi, M., Black, E., & Marsham, J. H. (2021). Extreme rainfall in East Africa, October 2019–January 2020 and context under future climate change. *Weather*, *76*(1), 26–31. https://doi.org/10.1002/wea.3824

Wang, J.-Z., Geng, T., Cai, W., Wang, G., Xie, M., Wu, L., & Chen, Z. (2024). Diverse responses of strong positive SST and rainfall Indian Ocean Dipole events under greenhouse warming. *Journal of Climate*, *37*(16), 4133–4151. https://doi.org/10.1175/JCLI-D-23-0631.1

Wang, J.-Z., & Wang, C. (2021). Joint boost to super El Niño from the Indian and Atlantic Oceans. *Journal of Climate*, *34*(12), 4937–4954. https://doi.org/10.1175/JCLI-D-20-0710.1

Wang, X., & Wang, C. (2014). Different impacts of various El Niño events on the Indian Ocean dipole. *Climate Dynamics*, *42*(3), 991–1005. https://doi.org/10.1007/s00382-013-1711-2

Webster, P. J., Moore, A. M., Loschnigg, J. P., & Leben, R. R. (1999). Coupled ocean–atmosphere dynamics in the Indian Ocean during 1997–98. *Nature*, *401*(6751), 356–360. https://doi.org/10.1038/43848

Wheeler, M. C., & Hendon, H. H. (2004). An all-season real-time multivariate MJO index: Development of an index for monitoring and prediction [Dataset]. *Monthly Weather Review*, *132*(8), 1917–1932. https://doi.org/10.1175/1520-0493(2004)132<1917:AARMMI>2.0.CO;2

Wright, R. (2023). Kenya: Millions displaced by the worst flooding in 100 years, Euronews. Retrieved from https://www.euronews.com/green/2023/12/15/floods-have-washed-away-entire-villages-kenyas-rains-made-twice-as-intense-by-climate-chan

Wyrtki, K. (1973). An equatorial jet in the Indian Ocean. *Science*, *181*(4096), 262–264. https://doi.org/10.1126/science.181.4096.262

Xie, P., & Arkin, P. A. (1997). Global precipitation: A 17-year monthly analysis based on gauge observations, satellite estimates, and numerical model outputs [Dataset]. *Bulletin of the American Meteorological Society*, *78*(11), 2539–2558. https://doi.org/10.1175/1520-0477(1997)078<2539:GPAYMA>2.0.CO;2

Yoshida, K. (1959). A theory of the cromwell current (the equatorial undercurrent) and of the equatorial upwelling—An interpretation in a similarity to a coastal circulation. *Journal of the Oceanographical Society of Japan*, *15*(4), 159–170. https://doi.org/10.5928/kaiyou1942.15.159

Zhang, L., Han, W., & Hu, Z.-Z. (2021). Interbasin and multiple-time-scale interactions in generating the 2019 extreme Indian Ocean Dipole. *Journal of Climate*, *34*(11), 4553–4566. https://doi.org/10.1175/JCLI-D-20-0760.1

Zhang, L., Han, W., Meehl, G. A., Hu, A., Rosenbloom, N., Shinoda, T., & McPhaden, M. J. (2021). Diverse impacts of the Indian Ocean Dipole on El Niño–Southern oscillation. *Journal of Climate*, *34*(22), 9057–9070. https://doi.org/10.1175/JCLI-D-21-0085.1

Zhang, L., Wang, G., Newman, M., & Han, W. (2021). Interannual to decadal variability of tropical Indian Ocean sea surface temperature: Pacific influence versus local internal variability. *Journal of Climate*, *34*(7), 2669–2684. https://doi.org/10.1175/JCLI-D-20-0807.1

Zhang, W., Wang, Y., Jin, F.-F., Stuecker, M. F., & Turner, A. G. (2015). Impact of different El Niño types on the El Niño/IOD relationship. *Geophysical Research Letters*, *42*(20), 8570–8576. https://doi.org/10.1002/2015GL065703

Zhao, Y., & Nigam, S. (2014). The Indian Ocean dipole: A monopole in SST. *Journal of Climate*, *28*(1), 3–19. https://doi.org/10.1175/JCLI-D-14-00047.1